

- Oceanogr.* **30**, 1 (1985).
12. S. Taguchi, G. R. DiTullio, E. A. Law, *Deep-Sea Res.* **35**, 8 (1988); T. R. Parsons, M. Takahashi, B. Hargrave, *Biological Oceanographic Processes* (Pergamon Press, Oxford, ed. 3, 1984).
 13. Feeding on zooplankton was assessed by dissection of 8625 individual polyps from 30 colonies, collected from the reef at different times during day and night and from areas with different flow speeds. Gut contents were extrapolated to daily rates of intake by the assumption of a digestion time of 6 hours [J. B. Lewis, *J. Zool.* **196**, 371 (1982)]. The estimate of the amount of carbon from zooplankton was based on J. Rodriguez and M. M. Mullin, *Limnol. Oceanogr.* **32**, 361 (1984): $\log W = 2.23 \times \log L - 5.58$, where W is the weight of carbon in micrograms and L is body length in micrometers. The very low number of zooplankton in the corals' gastrovascular cavities prevented recognition of possible effects of flow rates on capture rates.
 14. A known volume of water was pumped from 40 m offshore and 5 m water depth into a reservoir ashore and then gently passed through a 60- μm plankton net. Items were counted and body sizes determined by means of video image analysis. Zooplankton carbon values are most probably lower in yearly average than during the experiment (which was done in May), whereas phytoplankton carbon concentrations (measured in October) are higher at other seasons.
 15. One previous indication of herbivory in soft corals was a report of the presence of the plant-digesting enzymes amylase and laminarinase in three zooxanthellate soft corals (*Alcyonium*) during a broad-scale screening of carbohydrases in marine invertebrates [L. A. Elyakova, N. M. Shevchenko, S. M. Awaeva, *Comp. Biochem. Physiol.* **69**, 905 (1981)].
 16. R. C. Brusca and G. J. Brusca, *Invertebrates* (Sinauer, Sunderland, MA, 1990), p. 239.
 17. J. B. Lewis, *Biol. Rev.* **52**, 311 (1977). Gross productivity in the reefs around Eilat, Israel, is high with 12.3 g of carbon per square meter per day [D. J. Barnes and B. Lazar, *J. Exp. Mar. Biol. Ecol.* **174**, 7 (1993)].
 18. W. Hamner and J. Carleton, *Limnol. Oceanogr.* **24**, 1 (1979); J. L. Meyer, E. T. Schultz, G. S. Helfman, *Science* **220**, 1047 (1983).
 19. We are grateful to all staff and members of the H. Steinitz Marine Biology Laboratory of the Interuniversity Institut of Eilat, where this research was carried out. D. Klumpp, T. Ayukai, and C. Wilkinson critically read this manuscript. K.F. was supported by the German-Israeli Science foundation MINERVA. The research was funded by the Wolfson Foundation, administered by the Israel Academy of Science (grant to A.G.).

15 July 1994; accepted 30 January 1995

Native *Escherichia coli* OmpF Porin Surfaces Probed by Atomic Force Microscopy

Frank A. Schabert,* Christian Henn, Andreas Engel†

Topographs of two-dimensional porin OmpF crystals reconstituted in the presence of lipids were recorded in solution by atomic force microscopy (AFM) to a lateral resolution of 10 angstroms and a vertical resolution of 1 angstrom. Protein-protein interactions were demonstrated on the basis of the AFM results and earlier crystallographic findings. To assess protein-lipid interactions, the bilayer was modeled with kinked lipids by fitting the head groups to contours determined with AFM. Finally, two conformations of the extracellular porin surface were detected at forces of 0.1 nanonewton, demonstrating the potential of AFM to monitor conformational changes with high resolution.

The outer membrane protects the *Escherichia coli* cell against hostile agents and facilitates the uptake of nutrients (1). The latter activity is mediated by porins (2), of which matrix porin [OmpF (3)] is a major species. X-ray crystallography has resolved the atomic structure of this trimeric channel protein (4). The strands of the β barrel forming the pores are connected by short turns on the periplasmic surface and by loops of variable length on the extracellular surface. When reconstituted in the presence of phospholipids, OmpF porin assembles into various two-dimensional (2D) crystal forms. Electron microscopy of negatively stained, double-layered trigonal and rectangular crystals led to the 3D structure of the

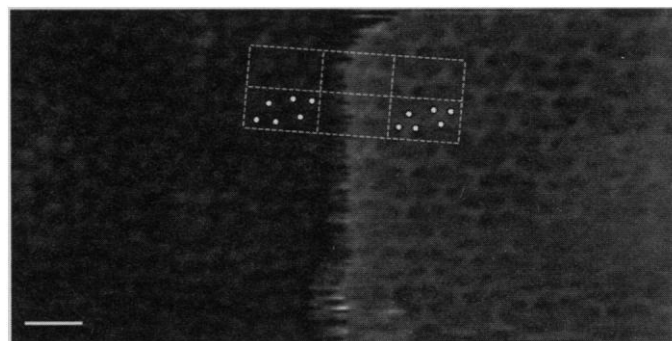
channel at a resolution of 20 Å (5).

In pursuit of our goal to acquire subnanometer-scale surface information of a membrane protein embedded in the lipid bilayer, we imaged 2D OmpF-phospholipid crystals adsorbed to freshly cleaved mica in

buffer solution by AFM (6). Double-layered rectangular OmpF crystals expose only the periplasmic surface to the aqueous environment (7). In a manner similar to the dissection of gap junctions (8), mechanical displacement of the top layer of crystals with the AFM stylus revealed the extracellular surface of the lower layer. Most likely as a result of electrostatic forces mediated by divalent cations, this lower layer remained firmly attached to the negatively charged mica surface (9). Steps at which the top layer broke off revealed both the corrugated extracellular surface (Fig. 1, left side) and the smooth periplasmic surface (Fig. 1, right side) of the porin trimer, as well as the packing of the two layers with respect to each other.

The periplasmic surface contains regularly arranged triplet channels that protrude less than 5 Å from the lipid surface. This surface was rather resistant to deformation by the stylus, reflecting the tight packing of the protein in the lipid bilayer. Thus, periplasmic surfaces could be scanned at least 10 times at forces below ~ 0.3 nN (9). Unprocessed topographs exhibit fine structural details (see Fig. 2A, left panel) that are enhanced by averaging (inset). The lateral resolution was determined to 8 Å by the Fourier ring correlation function (9). Quantitative analysis of the root-mean-square (rms) deviation of each pixel has revealed deviations smaller than 1 Å over the lipid moiety and the threefold symmetry axis of the trimer (9). To assess the accuracy of these topographical data, we generated a model of the 2D crystal taking into account the atomic structure of the porin trimer (4) and the position and orientation of the trimers within the unit cell as determined by AFM, without including the lipid bilayer. Averaged surface contours determined by AFM could thus be directly compared to the protein structure from x-ray analysis. As displayed in Fig. 2A (right panel), subtle features such as the three protrusions clustered about the threefold symmetry axes or

Fig. 1. Steps of the OmpF porin sheets imaged by AFM. The corrugated extracellular surface (left side) and the smooth periplasmic surface (right side) were visualized simultaneously at a loading force of 0.1 nN, after careful displacement of the upper layer. The topograph was recorded with a Nanoscope III (Digital Instruments, Santa Barbara, California) and oxide-sharpened Si_3N_4 tips on a 100- μm -long cantilever with a spring constant $k = 0.1$ N/m (Olympus Ltd., Tokyo, Japan). Rectangular unit cells ($a = 135$ Å and $b = 82$ Å) that comprise two trimers are framed. Small circles mark the trimers in unit cells on both extracellular and periplasmic surfaces. Scale bar, 10 nm. Topographs were recorded in 20 mM Hepes (pH 7.0), 100 mM NaCl, and 2 mM MgCl_2 .



Maurice E. Müller Institute for Microscopic Structural Biology, Biozentrum, Universität Basel, CH-4056 Basel, Switzerland.

*Present address: Institut für Physik, Lehrstuhl Physik von Makromolekülen, Humboldt-Universität zu Berlin, D-10115 Berlin, Germany.

†To whom correspondence should be addressed.

the distinct depression in the channel wall at the contact site of two adjacent trimers are in excellent agreement with the model. Major differences occur over the chan-

nels and where thin protein walls are aligned perpendicular to the fast scan direction, even at forces of 0.1 nN.

To obtain a resolution beyond 20 Å on

the extracellular surface of the porin crystal, the force of the stylus must be reduced to 0.1 nN (9). This requirement suggests that the extracellular domains that protrude by 11 ± 2 Å ($n = 130$) from the lipid bilayer are more flexible than observation by x-ray analysis revealed for an apparently frozen conformation (4). The corrugated surface shows deep trenches parallel to the lattice lines that pass through the threefold symmetry axes of the trimers, the sites at which the tip is lowered into the vestibule formed by the three extracellular domains (Figs. 1 and 2B, left panel). Probably as a result of its flexibility, the extracellular porin surface could not be imaged at a lateral resolution better than 13 Å. The experimental contours follow the model closely, in particular over protrusions where the difference is in general smaller than 1 Å (Fig. 2B, right panel).

Figure 3 shows the atomic scale model of the 2D porin crystal calculated from the atomic structure of the trimer (4) and the packing arrangement deduced from the topograph of Fig. 2A. Highly specific protein-protein interactions are seen that are likely to mediate the crystalline packing of porin trimers. Most prominent are potential salt bridges on the extracellular surface formed by lysines 25 and negatively charged carboxylates of adjacent trimers (Fig. 3A). Specific hydrophobic contacts may contribute to the stability of the periplasmic surface (Fig. 3B). Moreover, the vertical positions of the lipid head groups determined by AFM (Fig. 2) and the structure of kinked dimyristoyl phosphatidylcholine molecules (10) were used to model the lipid bilayer. As illustrated in Fig. 3C, this bilayer inter-

Fig. 2. Comparison of high-resolution AFM topographs representing the periplasmic and extracellular surface of 2D rectangular porin-phospholipid crystals with the model of the porin trimer derived from the atomic structure. (A) Topograph of the periplasmic surface (left panel). To eliminate friction artifacts, we added frames recorded in trace and retrace directions after lateral alignment (14), and lattice distortions were corrected by unbending (15). The average shown in the inset was calculated from 25 translationally aligned subframes. The lateral resolution of such topographs was determined to 8 to 15 Å, depending on the criteria (9). To allow comparison, the electron density based on the x-ray structure of the OmpF porin trimer at a resolution of 2.4 Å (4) was rendered at a lateral resolution of 15 Å, including the entire trimer mass. Position and orientation of the porin trimers were determined from the average (inset) to generate a model of the protein within the 2D crystal (red). Zebra-like contours (dark and light blue) on the overlaid transparent AFM topograph mark zones of identical altitude, with a height difference between contours of 1 Å. The thickness of a single layer, 61 ± 2 Å ($n = 224$), was measured at steps such as those shown in Fig. 1 and was used for the vertical positioning of the AFM topographs relative to the model. A distinct depression in the channel wall is encircled. (B) The sum of trace and retrace signal from the extracellular surface (left panel) exhibits prominent rows of protrusions separated by trenches running at approximately 45°. The average (inset) shows the three protrusions of the trimer in the center surrounded by adjacent trimers. Angular and translational alignment of the average with the crystal model shown in (A) after its rotation by π about the y axis yielded the overlay for the extracellular surface (right panel). Insets are displayed at identical magnification and aligned with respect to the unprocessed data. In panels on the right, triangles mark the threefold axis of an individual porin trimer, whereas the scanning direction is indicated with double-headed arrows. Scale bar, 10 nm.

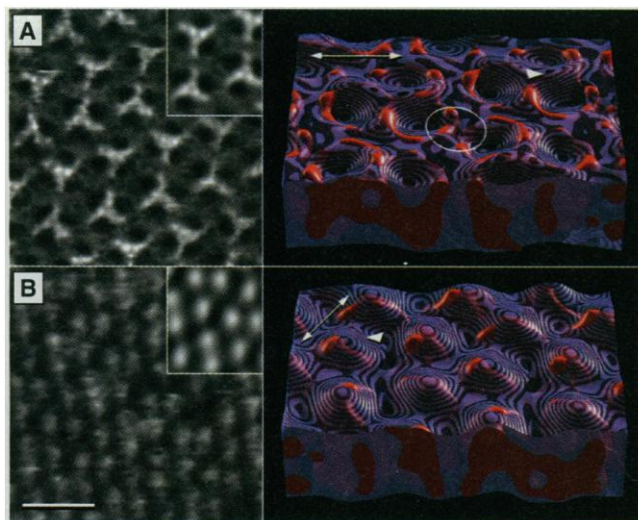
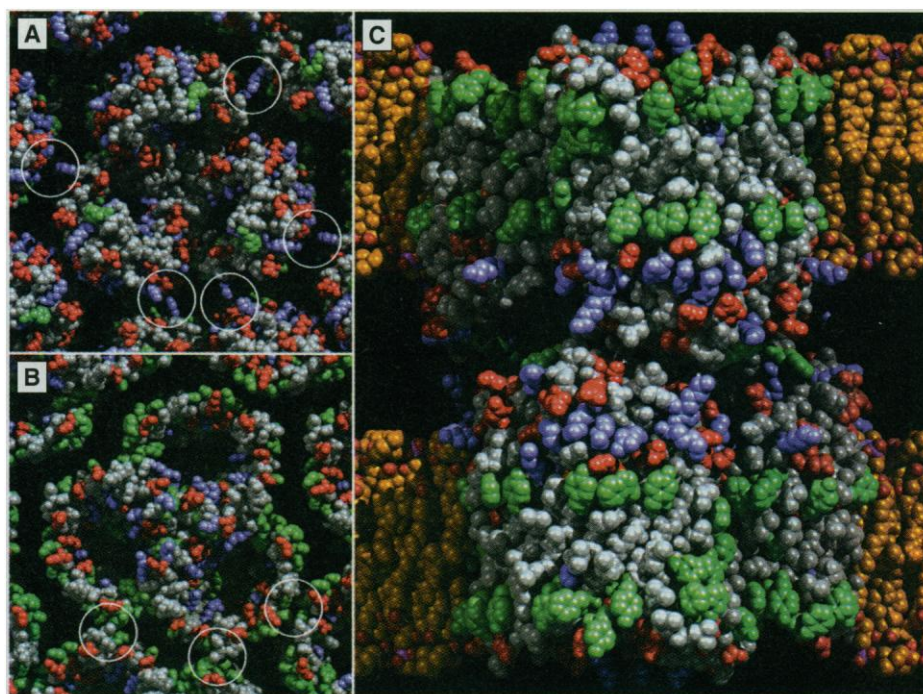


Fig. 3. Atomic models of protein-protein and lipid-protein interactions based on the x-ray structure of the porin trimer (4) and the topographs recorded by AFM. (A) The extracellular surface exhibits a salt bridge pattern between lysines 25 and negatively charged carboxyl groups of neighboring trimers (circled). (B) In contrast, protein-protein interactions on the periplasmic surface appear to be of a hydrophobic nature. (C) To generate a model of the double layer, we derived the relative orientation and position of the top and bottom layers from Fig. 1. Accordingly, extracellular surfaces are apposed and the two layers are related by a two-fold screw axis along lattice vector a . The vertical position of the top layer was adjusted by rigid body-fitting to reveal a perfect match of the topographies of the two adjacent trimers. Rigid lipid molecules were modeled in their shortest possible kinked conformation (10). Taking their vertical positions from the topographs shown in Fig. 2, we brought lipid molecules into van der Waals contact with the trimer surface. Minor adjustments (<2 Å) were required on the extracellular surface to establish a symmetric arrangement of the bilayer relative to the rings of aromatic residues. Color coding: red, negatively charged; blue, positively charged; green, aromatic; dark gray, all other types of amino acids; and yellow, lipid carbons.



acts mainly with the hydrophobic belt delimited by two rings of aromatic residues, consistent with the hypothesis proposed by Cowan and co-workers (4). In addition, the close fit of intercalating extracellular domains documented in Fig. 3C is responsible for the ordered interlayer interaction of double-layered 2D crystals.

We observed that the extracellular porin surface may exist in two conformations. This finding is rare but reproducible, consisting of a 5 Å shift of the extracellular domains to-

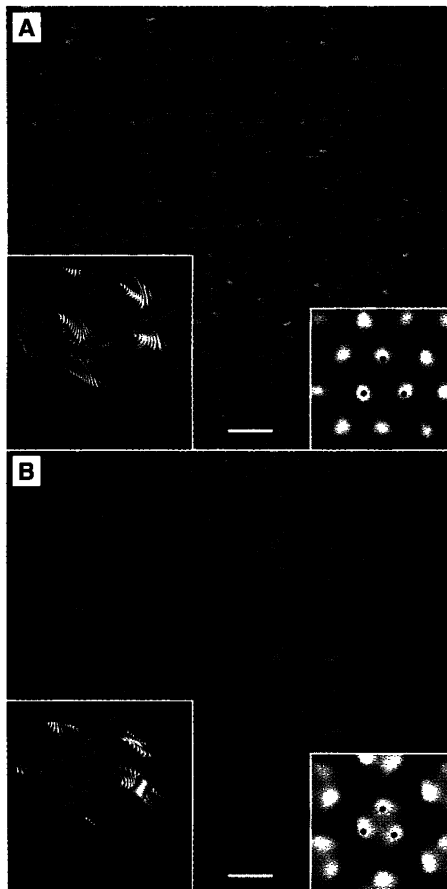


Fig. 4. Two conformations of the OmpF porin as identified by AFM are compared to the model derived from the atomic structure. **(A)** Raw data of a trigonal 2D crystal that exhibits the characteristic morphology of the extracellular porin trimer surface. The overlay shown in the lower left corner of AFM data (transparent, in dark and light blue) and the trimer model (opaque, red) were generated from the threefold symmetrized average (inset, lower right corner). **(B)** A different morphology recorded with the same stylus on the same trigonal crystal as in (A). Trace and retrace scans were merged. Small patches with prominent trimeric protrusions arranged on an undistorted lattice were found embedded within a topography corresponding to that displayed in (A). The comparison of the threefold symmetrized average (inset, right) with the model (inset, left; colors as above) shows that the extracellular domains are shifted by 5 Å toward the threefold axis of the porin trimer. The centers of the protrusions are indicated with red dots. Scale bars in (A) and (B), 10 nm.

ward the center of the trimer (compare Fig. 4A with Fig. 4B). Although energy requirements cannot be estimated from a static atomic structure (4), the displacement observed appears sterically possible and would constrict the channel entrances. This may explain the two open-channel configurations of *E. coli* porins (11, 12).

As demonstrated here, the comparison of the structural data from x-ray crystallography with those from AFM contributes a new insight into the structure of lipids in biological membranes. Also, because 2D crystals of membrane proteins are more easily produced than 3D crystals, the combination of cryoelectron microscopy and AFM may be an attractive alternative. Finally, the two conformations of the extracellular surface of OmpF porin (Fig. 4) and the recent report on conformational fluctuations of active lysozyme (13) suggest that the atomic force microscope may become an essential tool in monitoring function-related conformational changes.

REFERENCES AND NOTES

1. H. Nikaido and M. Vaara, *Microbiol. Rev.* **49**, 1 (1985).
2. B. K. Jap and P. J. Walian, *Q. Rev. Biophys.* **23**, 367 (1990).

3. J. P. Rosenbusch, *J. Biol. Chem.* **249**, 8019 (1974).
4. S. W. Cowan *et al.*, *Nature* **358**, 727 (1992).
5. A. Engel, A. Massalski, H. Schindler, D. L. Dorset, J. P. Rosenbusch, *ibid.* **317**, 643 (1985).
6. G. Binnig, C. F. Quate, Ch. Gerber, *Phys. Rev. Lett.* **56**, 930 (1986).
7. A. Hoenger, J.-M. Pagès, D. Fourel, A. Engel, *J. Mol. Biol.* **233**, 400 (1993).
8. J. H. Hoh, R. Lal, S. A. John, J.-P. Revel, M. F. Amsdorf, *Science* **253**, 1405 (1991).
9. F. Schabert and A. Engel, *Biophys. J.* **67**, 2394 (1994).
10. A. Seelig and J. Seelig, *Biochemistry* **13**, 4893 (1974).
11. J. C. Todt, W. J. Rocque, E. J. McGroarty, *ibid.* **31**, 10471 (1992).
12. L. K. Buehler, S. Kusumoto, H. Zhang, J. P. Rosenbusch, *J. Biol. Chem.* **266**, 24446 (1991).
13. M. Radmacher, M. Fritz, H. G. Hansma, P. K. Hansma, *Science* **265**, 1577 (1994).
14. M. Radmacher, R. W. Tilmann, M. Fritz, H. E. Gaub, *ibid.* **257**, 1900 (1992).
15. W. O. Saxton, R. Dürr, W. Baumeister, *Ultramicroscopy* **46**, 287 (1992).
16. We thank U. Aebi, J. P. Rosenbusch, and C. A. Schönberger for constructive discussions of the manuscript and T. Schirmer for evaluating steric constraints in the observed conformational change of extracellular OmpF domains. This work was supported by the Swiss National Foundation for Scientific Research, grant 31-32536.91 to A.E.; by the Department of Education of Basel-Stadt; by the research foundations of Ciba, Hoffmann-La Roche, and Sandoz; and by the Maurice E. Müller Foundation of Switzerland.

10 November 1994; accepted 9 February 1995

A Morbillivirus That Caused Fatal Disease in Horses and Humans

Keith Murray,* Paul Selleck, Peter Hooper, Alex Hyatt, Allan Gould, Laurie Gleeson, Harvey Westbury, Lester Hiley, Linda Selvey, Barry Rodwell, Peter Ketterer

A morbillivirus has been isolated and added to an increasing list of emerging viral diseases. This virus caused an outbreak of fatal respiratory disease in horses and humans. Genetic analyses show it to be only distantly related to the classic morbilliviruses rinderpest, measles, and canine distemper. When seen by electron microscopy, viruses had 10- and 18-nanometer surface projections that gave them a "double-fringed" appearance. The virus induced syncytia that developed in the endothelium of blood vessels, particularly the lungs.

The emergence of new viruses may result in previously unrecognized or new diseases (1–3). Although emerging viruses may contain novel mutations or represent gradual evolu-

K. Murray, P. Selleck, P. Hooper, A. Hyatt, A. Gould, L. Gleeson, H. Westbury, CSIRO Australian Animal Health Laboratory, Fyrie Street, East Geelong, Victoria 3220, Australia.

L. Hiley, Queensland Department of Health, Centre for Public Health Sciences, 63 George Street, Brisbane 4000, Queensland, Australia.

L. Selvey, Communicable Diseases, Queensland Health, 160 Mary Street, Brisbane 4000, Queensland, Australia. B. Rodwell and P. Ketterer, Queensland Department of Primary Industries, Animal Research Institute, Yeerongpilly 4105, Queensland, Australia.

*To whom correspondence should be addressed.

tion (3), more often they emerge because of changes in behavior or the environment whereby they are introduced to a new host (3–5). Viruses that are pathogenic in novel human and nonhuman hosts include Marburg and Ebola viruses; hantaviruses; human immunodeficiency viruses; Lassa virus; dolphin, porpoise, and phocine morbilliviruses; feline immunodeficiency virus; and bovine spongiform encephalopathy agent (3).

Dolphin, porpoise, and phocine morbilliviruses, rinderpest virus, and measles virus belong to the genus *Morbillivirus* within the family Paramyxoviridae. Although nonhuman morbilliviruses have been associated